Geophysical Journal International

Geophys. J. Int. (2012) **191,** 175–188 doi: 10.1111/j.1365-246X.2012.05593.x

Seismic waves estimation and wavefield decomposition: application to ambient vibrations

Stefano Maranò,[1] Christoph Reller,[2] Hans-Andrea Loeliger[2] and Donat Fäh[1]

[1] *ETH Zurich, Swiss Seismological Service,* 8092 *Zürich, Switzerland. E-mail: marano@sed.ethz.ch*
[2] *ETH Zurich, Department of Information Technology & Electrical Engineering,* 8092 *Zürich, Switzerland*

Accepted 2012 June 27. Received 2012 June 27; in original form 2011 August 7

SUMMARY

Passive seismic surveying methods represent a valuable tool in local seismic hazard assessment, oil and gas prospection, and in geotechnical investigations. Array processing techniques are used in order to estimate wavefield properties such as dispersion curves of surface waves and ellipticity of Rayleigh waves. However, techniques presently in use often fail to properly merge information from three-components sensors and do not account for the presence of multiple waves. In this paper, a technique for maximum likelihood estimation of wavefield parameters including direction of propagation, velocity of Love waves and Rayleigh waves, and ellipticity of Rayleigh waves is described. This technique models jointly all the measurements and all the wavefield parameters. Furthermore it is possible to model the simultaneous presence of multiple waves. The performance of this technique is evaluated on a high-fidelity synthetic data set and on real data. It is shown that the joint modelling of all the sensor components, decreases the variance of wavenumber estimates and allows the retrieval of the ellipticity value together with an estimate of the prograde/retrograde motion.

Key words: Time-series analysis; Surface waves and free oscillations.

1 INTRODUCTION

Analysis of the seismic wavefield enables us to gather knowledge of geological and geophysical features of the subsoil. Indeed seismic wave attributes such as velocity of propagation or polarization reflect the properties of the structure in which the wave is propagating. The analysis of these properties allow geophysicists to gain insight into the subsoil avoiding more expensive invasive techniques (e.g. borehole techniques). Seismic surveying methods represent a valuable tool in oil and gas prospection (Sheriff & Geldart 1995) and in geophysical investigations (Tokimatsu 1997; Okada 1997).

In this paper, we present an application to *ambient vibrations* of a recently proposed technique for the analysis of the seismic wavefield (Maranò *et al.* 2011). Ambient vibrations are seismic waves generated by natural or anthropogenic sources such as ocean waves, atmospheric changes or traffic (Bonnefoy-Claudet *et al.* 2006b) which are exploited in passive seismic methods. The advantage of passive methods is their applicability to urbanized areas and the ability to analyse lower frequencies that cannot be excited with active techniques, thus allowing to resolve deeper structures in the earth (Okada 1997).

In the case of a structure with low-velocity sediments above rock, the seismic wavefield of ambient vibrations is primarily composed of surface waves. But other waves are present such as body waves and resonances. In particular, the seismic wavefield is composed of an unknown number of simultaneously present waves of different type. In this work we focus on the analysis of surface waves, the interest lies in estimating the frequency dependence of the velocity and wave polarization. Specifically, we are interested in retrieving the dispersion relation for both Love wave and Rayleigh wave, and Rayleigh wave ellipticity.

To infer subsurface features of the earth, it is necessary to solve a geophysical inverse problem, see e.g. Tarantola (2004). The properties of the seismic wavefield deduced from seismic surveys are used in such an inverse problem.

For the analysis of surface waves from ambient vibrations, a planar sensor array is typically deployed and array processing techniques are employed. Most of the array processing techniques in use assume planar wave fronts. In particular, frequency-domain beamforming techniques can be used. Central to these methods is the estimation of the spectral spatial covariance matrix, see e.g. Van Trees (2002).

Two well-known techniques are the classical beamforming, or Bartlett method (Lacoss *et al.* 1969), and the high-resolution beamforming, or Capon method (Capon 1969). In both techniques signals from different sensors are delayed and summed up. Delays are computed as a function of angle of arrival and velocity of propagation. The final estimates of these two parameters are the values that maximize the sum. In the Capon method the sum is weighted by complex gains in order to reduce the impact of noise and the disturbance from interfering signals.

Another technique that found application in the seismological community is the MUSIC algorithm (Schmidt 1986). In this method an eigendecomposition of the spectral spatial covariance matrix

is performed and properties of the noise subspace are exploited. Cornou *et al.* (2003) have used the MUSIC algorithm for the analysis of ambient vibrations.

Single station approaches employing the three components of a triaxial seismometer exist (Christoffersson *et al.* 1988). In array processing, however, for a long time only the vertical component has been used. In recent work (Fäh *et al.* 2008), a technique was proposed to analyse also the horizontal components. The technique allows to distinguishing between Love waves and Rayleigh waves. Vertical and horizontal components are however processed separately, leading to sub optimal performances. Further work proposes a method for the estimation of Rayleigh wave ellipticity (Poggi & Fäh 2010). Also this latter work lacks of a joint treatment of all the three components.

In this paper, we describe a recently developed technique to perform maximum likelihood (ML) parameter estimation of wave parameters (Maranò *et al.* 2011). This technique models jointly the measurements from all components and all the parameters. It will be shown that this leads to a substantial improvement in the retrieval of the dispersion curves. In addition, an estimate of Rayleigh wave ellipticity including the sense of rotation of the particle is provided. We believe that this new information will provide a valuable additional constraint for the geophysical inversion. The technique also allows to address the issue of multiple waves by means of wavefield decomposition within the same framework leading to a more accurate parameter estimation and the detection of weaker waves. We assess the performance of the proposed technique on the ambient vibrations wavefield, both on high-fidelity synthetics and on real data, and compare with classical beamforming (Bartlett method).

The paper is organized as follows. In Section 2, we introduce our notation thereby recalling the wave equations of the displacement field induced by Love waves and Rayleigh waves, and we elaborate on the representation of Rayleigh wave ellipticity. In the same section we also define the estimation problem addressed in this paper. In Section 3, we present the technique central to this paper emphasizing its novel contributions. In Section 4, we provide numerical examples of the analysis of ambient vibrations from both high fidelity synthetics and real data. In Section 5, we summarize our contributions.

2 SYSTEM MODEL AND PROBLEM STATEMENT

2.1 Seismic surface waves

To measure seismic waves, we deploy an array of triaxial seismometers on the surface of the earth. We restrict our interest to small aperture arrays and work with a flat earth model. We use a 3-D, right-handed Cartesian coordinate system with the z axis pointing upward. The azimuth ψ is measured counter-clockwise from the x-axis. Each sensor measures the ground velocity along the direction of the axes of the coordinate system x, y, and z. We say that each sensor has three components, each component measuring the motion of the ground along a certain direction. For the sake of simplicity, we provide wave equations of the displacement field $\boldsymbol{u}$, despite the actual measurement is the velocity field $\frac{\partial \boldsymbol{u}}{\partial t}$. The displacement field, at position $\boldsymbol{p} \in \mathbb{R}^3$ and time t can be described by the vector field

$$\boldsymbol{u}(\boldsymbol{p}, t) = \big(u_x(\boldsymbol{p}, t), u_y(\boldsymbol{p}, t), u_z(\boldsymbol{p}, t)\big) : \mathbb{R}^4 \to \mathbb{R}^3 .$$

In this paper, we study waves propagating near the surface of the earth and having a direction of propagation lying on the horizontal plane $z = 0$. We consider the wavefield to be composed of the superposition of several Love waves and Rayleigh waves. The wave equations we describe hereafter are valid for $z = 0$ and for plane wave fronts. The direction of propagation of a wave is given by the wave vector $\boldsymbol{\kappa} = \kappa\,(\cos\psi, \sin\psi, 0)^{\mathrm{T}}$, whose length κ is the wavenumber.

Love waves exhibit a particle motion confined to the horizontal plane. The particle oscillates perpendicular to the direction of propagation. The particle displacement generated by a single Love wave at position and time $(\boldsymbol{p}, t)$ is

$$\begin{aligned} u_x(\boldsymbol{p}, t) &= -\alpha \sin\psi \cos\left(\omega t - \boldsymbol{\kappa}^{\mathrm{T}}\boldsymbol{p} + \varphi\right) \\ u_y(\boldsymbol{p}, t) &= \alpha \cos\psi \cos\left(\omega t - \boldsymbol{\kappa}^{\mathrm{T}}\boldsymbol{p} + \varphi\right) \\ u_z(\boldsymbol{p}, t) &= 0 . \end{aligned} \tag{1}$$

Rayleigh waves exhibit an elliptical particle motion confined to the vertical plane perpendicular to the surface of the earth and containing the direction of propagation of the wave. The particle displacement generated by a single Rayleigh wave is

$$\begin{aligned} u_x(\boldsymbol{p}, t) &= \alpha \sin\xi \cos\psi \cos\left(\omega t - \boldsymbol{\kappa}^{\mathrm{T}}\boldsymbol{p} + \varphi\right) \\ u_y(\boldsymbol{p}, t) &= \alpha \sin\xi \sin\psi \cos\left(\omega t - \boldsymbol{\kappa}^{\mathrm{T}}\boldsymbol{p} + \varphi\right) \\ u_z(\boldsymbol{p}, t) &= \alpha \cos\xi \cos\left(\omega t - \boldsymbol{\kappa}^{\mathrm{T}}\boldsymbol{p} + \pi/2 + \varphi\right) . \end{aligned} \tag{2}$$

We call $\xi \in [-\pi/2, \pi/2]$ *ellipticity angle* of the Rayleigh wave. This quantity determines the eccentricity and the sense of rotation of the particle motion. If $\xi \in (-\pi/2, 0)$, the Rayleigh wave elliptical motion is said to be *retrograde* (i.e. the oscillation on the vertical component u_z is shifted by $+\pi/2$ radians with respect to the oscillation on the direction of propagation). If $\xi \in (0, \pi/2)$ the wave is said to be *prograde*. For $\xi = 0$ and $\xi = \pm\pi/2$ the polarization is vertical and horizontal, respectively. The quantity $|\tan\xi|$ is known as the *ellipticity* of the Rayleigh wave.

We now explain in more detail the parametrization of ellipticity used to model Rayleigh waves as used in eq. (2). Commonly, Rayleigh wave ellipticity is referred to as the ratio of the absolute values of the amplitude on the radial component and on the vertical component, that is, the H/V ratio. Considering equation eq. (2), and defining $\mathrm{H} = |\alpha \sin\xi|$ and $\mathrm{V} = |\alpha \cos\xi|$ it follows that

$$\frac{\mathrm{H}}{\mathrm{V}} = \frac{|\alpha \sin\xi|}{|\alpha \cos\xi|} = |\tan\xi| .$$

Note that there is no information about the sense of rotation of the particle in the H/V ratio as the sign of $\tan\xi$ is lost. By considering directly the ellipticity angle ξ it is possible to preserve this information and infer the sense of particle rotation.

Fig. 1 depicts the two different representations for Rayleigh wave ellipticity in the case of a layer over a half space and clarifies this idea. Namely, the SESAME structural model M2.1 (Bard 2008; Bonnefoy-Claudet *et al.* 2006a) is used (see also Table 1). It is known that in such a model the motion of the fundamental mode is retrograde at low frequencies (Malischewsky *et al.* 2008, 2006). At each singularity (i.e. $\mathrm{H} = 0$ or $\mathrm{V} = 0$) the sense of rotation changes from retrograde to prograde or vice versa. First, we look at the fundamental mode (solid red line) in the H/V representation of Fig. 1(a). The particle motion is retrograde up to 2 Hz, where the first singularity occurs and the particle motion is horizontally polarized. Between 2 and 3.8 Hz the particle motion is prograde, and at 3.8 Hz the wave is vertically polarized. Above 3.8 Hz the motion is again retrograde.

We stress that from this picture it is not possible to get any information about the sense of rotation of the particle and we are able to draw the above conclusions only because of our knowledge

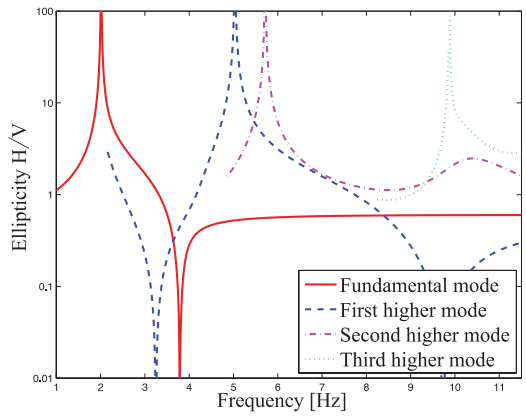

(a) Rayleigh wave ellipticity curve in the common H/V representation.

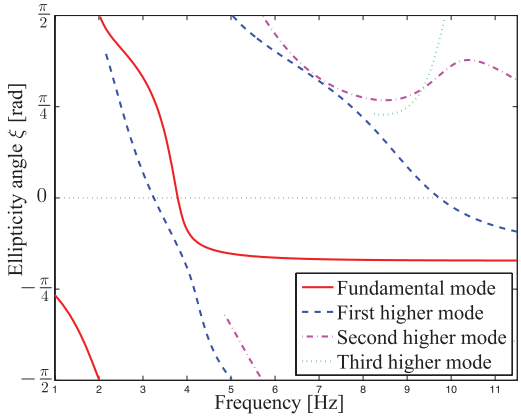

(b) Rayleigh wave ellipticity curve in the ellipticity angle ξ representation.

Figure 1. Two different representations of Rayleigh wave ellipticity in a layer over a half-space model.

Table 1. Details of the SESAME structural model M2.1.

	v_p [m s^{-1}]	v_s [m s^{-1}]	Q_p	Q_s	ρ [kg m^{-3}]	Thickness [m]
Layer 1	500	200	50	25	1900	25
Layer 2	2000	1000	100	50	2500	∞

about the structural model. In Fig. 1(b) the ellipticity is represented by means of the ellipticity angle ξ. As explained earlier in this section, the particle motion is retrograde when $\xi \in (-\pi/2, 0)$ and it is prograde when $\xi \in (0, \pi/2)$. The polarization is vertical for $\xi = 0$ and horizontal for $\xi = \pm\pi/2$. Similar considerations can be made for the higher modes. This latter representation of Rayleigh wave ellipticity allows to visualize the sense of rotation of the wave.

2.2 Problem statement

Our end goal lies in the estimation of wavefield parameters $\boldsymbol{\theta}$ based on noisy measurements $\boldsymbol{y}$ from an array of seismometers. For a Love wave we define the parameter vector $\boldsymbol{\theta}^{(\mathrm{L})} \triangleq (\alpha, \varphi, \kappa, \psi)$. For a Rayleigh wave we define $\boldsymbol{\theta}^{(\mathrm{R})} \triangleq (\alpha, \varphi, \kappa, \psi, \xi)$. First, we are interested in computing the likelihood $p(\boldsymbol{y}|\boldsymbol{\theta})$ of the measurements $\boldsymbol{y}$ given a specific parameter vector $\boldsymbol{\theta}$. Second, these likelihood computations enable us to perform ML parameter estimation.

The seismic wavefield is composed of multiple, simultaneously present, waves. This interference can downgrade the quality of the result of the analysis. In this work, we propose an approach, called wavefield decomposition, enabling us to separate the contribution of different waves and improving the accuracy of the parameter estimation.

In addition, we assume the noise variance to be different on each sensor and on each sensor component. Therefore, we are interested in estimating these noise variances. In the estimation of wavefield parameters, more weight is given to sensors with smaller noise variance and less weight to noisy sensors.

3 PROPOSED TECHNIQUE

3.1 Overview

In the proposed technique we devise a statistical model of the seismic wavefield thereby tackling the superposition of an unknown number of waves of different type. In this section, we describe how the algorithm deals with:

(i) Wavefield parameters estimation in the single wave setting.
(ii) Wavefield parameters estimation in the multiple wave setting.
(iii) Wave type choice.
(iv) Determination of the number of waves.
(v) Noise variance estimation.

In the final application, different frequencies are processed separately and a long recording is split in shorter time windows. The composition of the wavefield is allowed to change at different frequencies and in different time windows. In this section, we describe the modelling of multiple monochromatic waves with the same frequency. The wavefield composition (i.e. the number and the type of waves) is assumed to remain unchanged within each time window.

An informal high-level description of the operating principle of the proposed method is provided in Algorithm 1.

3.2 Maximum likelihood parameter estimation

Our interest lies in computing the likelihood of the observations $\boldsymbol{y}$ for a specific wave type and wave parameter vector $\boldsymbol{\theta}$. Then a maximization of the likelihood function enables us to perform ML parameter estimation.

We rely on noisy measurements from L channels. In the case of N three-components sensors, we have $L = 3N$. In particular, on the ℓ-th channel the measurements $Y_k^{(\ell)}$ at discrete instants t_k for $k = 1, \ldots, K$ are

$$Y_k^{(\ell)} = u(\boldsymbol{p}_\ell, t_k) + Z_k^{(\ell)},$$

where $u(\boldsymbol{p}_\ell, t_k)$ is a deterministic function of unknown wavefield parameters $\boldsymbol{\theta}$ and $Z_k^{(\ell)}$ is zero-mean additive white Gaussian noise with variance σ_ℓ^2. With this signal model, the probability density function (PDF) of the observations $\boldsymbol{y}$ is

$$p(\boldsymbol{y}|\boldsymbol{\theta}) = \prod_{\ell=1}^{L}\prod_{k=1}^{K} \frac{1}{\sqrt{2\pi\sigma_\ell^2}} \mathrm{e}^{-\left[y_k^{(\ell)} - u(\boldsymbol{p}_\ell, t_k)\right]^2 / 2\sigma_\ell^2}, \tag{3}$$

where we have grouped all the measurement as $\boldsymbol{y} = \{y_k^{(\ell)}\}_{l=1,\ldots,L}^{k=1,\ldots,K}$.

Observe that, for a given wave type, $u(\boldsymbol{p}_\ell, t_k)$ is a deterministic function of the wavefield parameters $\boldsymbol{\theta}$ for each ℓ and k. This function is written explicitly in eqs (1) and (2). The ML estimate

Algorithm 1. High-level description of the proposed method.

1. $M_{\max} \leftarrow$ Maximum number of waves.
   {Initial estimate for σ_ℓ^2:}
2. **for** $\ell = 1$ to L **do**
3. $\quad \hat{\sigma}_\ell^2 = \frac{1}{K}\sum_{k=1}^{K}(y_k^{(\ell)})^2$
4. **end for**
   {Increase the number of waves from 1 to at most $M_{\max}$:}
5. **for** $m = 1$ to $M_{\max}$ **do**
6. Compute BIC for a model of $m-1$ waves.
   {For all the possible wave types (e.g. Rayleigh, Love) fit the m-th wave:}
7. **for all** T $= \{$R, L$\}$ **do**
8. **repeat**
9. $\quad \hat{\boldsymbol{\theta}}_m^{(\mathrm{T})} = \operatorname{argmax}_{\boldsymbol{\theta}_m} p(\boldsymbol{y}|\hat{\boldsymbol{\theta}}_1, \ldots, \hat{\boldsymbol{\theta}}_{m-1}, \boldsymbol{\theta}_m^{(\mathrm{T})}, \hat{\sigma}_1^2, \ldots, \hat{\sigma}_L^2)$
10. $\quad \left(\hat{\sigma}_1^2, \ldots, \hat{\sigma}_L^2\right) = \operatorname{argmax}_{(\sigma_1^2,\ldots,\sigma_L^2)} p(\boldsymbol{y}|\hat{\boldsymbol{\theta}}_1, \ldots, \hat{\boldsymbol{\theta}}_m, \sigma_1^2, \ldots, \sigma_L^2)$
11. **until** convergence of $p(\boldsymbol{y}|\hat{\boldsymbol{\theta}}_1, \ldots, \hat{\boldsymbol{\theta}}_m, \hat{\sigma}_1^2, \ldots, \hat{\sigma}_L^2)$.
12. Compute BIC for a model of m waves.
13. **end for**
14. Choose model with smallest BIC. Potentially, stop adding waves and exit.
    {Refine estimation of existing waves:}
15. **repeat**
16. **for** $i = 1$ to m **do**
17. $\quad \hat{\boldsymbol{\theta}}_i = \operatorname{argmax}_{\boldsymbol{\theta}_i} p(\boldsymbol{y}|\hat{\boldsymbol{\theta}}_1, \ldots, \hat{\boldsymbol{\theta}}_{i-1}, \boldsymbol{\theta}_i, \hat{\boldsymbol{\theta}}_{i+1}, \ldots, \hat{\boldsymbol{\theta}}_m, \hat{\sigma}_1^2, \ldots, \hat{\sigma}_L^2)$
18. **end for**
19. $\left(\hat{\sigma}_1^2, \ldots, \hat{\sigma}_L^2\right) = \operatorname{argmax}_{(\sigma_1^2,\ldots,\sigma_L^2)} p(\boldsymbol{y}|\hat{\boldsymbol{\theta}}_1, \ldots, \hat{\boldsymbol{\theta}}_m, \sigma_1^2, \ldots, \sigma_L^2)$
20. **until** convergence of $p(\boldsymbol{y}|\hat{\boldsymbol{\theta}}_1, \ldots, \hat{\boldsymbol{\theta}}_m, \hat{\sigma}_1^2, \ldots, \hat{\sigma}_L^2)$.
21. **end for**

$\hat{\boldsymbol{\theta}}$ of the parameter vector $\boldsymbol{\theta}$ is obtained by means of the following maximization

$$\hat{\boldsymbol{\theta}} = \operatorname*{argmax}_{\boldsymbol{\theta}} p\left(\boldsymbol{y}\middle|\boldsymbol{\theta}\right).$$

This suffices to estimate wave parameters in the single wave setting. More details on ML estimation can be found, for example, in Kay (1993).

3.3 Wavefield decomposition

In the seismic wavefield several waves of different functional form are present simultaneously. This superposition can severely downgrade the quality of the estimation process if not addressed appropriately. In this work, we propose an approach, called wavefield decomposition, enabling us to separate the contribution of different waves and improving the accuracy of the parameter estimation.

Assuming a linear medium, each sensor records the linear superposition of such waves. Therefore, in presence of M waves, we have that the measurement $Y_k^{(\ell)}$ is

$$Y_k^{(\ell)} = \sum_{m=1}^{M} u^{(m)}(\boldsymbol{p}_\ell, t_k) + Z_k\,,$$

where $u^{(m)}(\boldsymbol{p}_\ell, t_k)$ is the contribution of the m-th wave.

It follows immediately, that in the multiple wave setting, the PDF (3) should be altered by replacing $u(\boldsymbol{p}_\ell, t_k)$ by $\sum_{m=1}^{M} u^{(m)}(\boldsymbol{p}_\ell, t_k)$. The PDF is now parametrized by several wavefield parameter vectors, $(\boldsymbol{\theta}_1, \ldots, \boldsymbol{\theta}_M)$.

In principle, also in the multiple wave setting it is possible to obtain wave parameter estimates by maximizing

$$\left(\hat{\boldsymbol{\theta}}_1, \ldots, \hat{\boldsymbol{\theta}}_M\right) = \operatorname*{argmax}_{(\boldsymbol{\theta}_1,\ldots,\boldsymbol{\theta}_M)} p(\boldsymbol{y}|\boldsymbol{\theta}_1, \ldots, \boldsymbol{\theta}_M)\,.$$

Unfortunately, such a maximization is unfeasible, even for small M, because the parameter space is increased M-fold.

Therefore we propose a greedy algorithm that increases gradually the number of waves modelled. The algorithm begins modelling a single wave and estimates the parameter vector $\boldsymbol{\theta}_1$ of the first wave. This wave can be either a Love wave or a Rayleigh wave. In a second step, the parameters of the first wave are kept fixed to $\hat{\boldsymbol{\theta}}_1$ while the maximization is performed over $\boldsymbol{\theta}_2$. The number of waves modelled by the algorithm is increased gradually until a stopping criterion is reached. Each estimated parameter vector benefits from the estimation of the other waves as the parameter estimation is repeated iteratively.

3.4 Model selection

Two questions arising naturally are how to choose the wave type and how many waves should be modelled. Both questions pertains to model selection. We employ the Bayesian information criterion (BIC) for this task (Schwarz 1978).

The BIC is used both to select the wave type and to stop the from modelling additional waves. Considering a set of possible models, differing for wave type and number of waves, the model with the smallest BIC is selected. The BIC is defined as

$$\mathrm{BIC} = -2p\left(\boldsymbol{y}\middle|\hat{\boldsymbol{\theta}}_1, \ldots, \hat{\boldsymbol{\theta}}_M\right) + N_p \ln(LK)\,,$$

where N_p denotes the total number of estimated parameters of the model and LK is the number of measurements.

In order to limit the computational complexity of the proposed method, we set the number of waves jointly modelled to be at most $M_{\max}$.

3.5 Noise variance estimation

We assume the measurements to be corrupted by additive white Gaussian noise with zero mean. However, we do not assume the noise variance to be equal in different sensors or components. The estimation algorithm properly weights measurements from channels with different noise level.

An ML estimate of noise variance can be obtained with the following maximization

$$\left(\hat{\sigma}_1^2, \ldots, \hat{\sigma}_L^2\right) = \underset{\left(\sigma_1^2, \ldots, \sigma_L^2\right)}{\operatorname{argmax}} \; p\left(\boldsymbol{y} \middle| \hat{\boldsymbol{\theta}}_1, \ldots, \hat{\boldsymbol{\theta}}_M, \sigma_1^2, \ldots, \sigma_L^2\right),$$

where the wavefield parameters are kept fixed and the maximization is performed only on the $\{\sigma_\ell^2\}_{\ell=1,\ldots,L}$. Because of the signal model, it is equivalent to perform L separate maximizations on σ_ℓ^2 for $\ell = 1, \ldots, L$.

Since the wavefield parameter estimates are influenced by the different noise variances we iteratively repeat the two maximizations

$$\left(\hat{\sigma}_1^2, \ldots, \hat{\sigma}_L^2\right) = \underset{\left(\sigma_1^2, \ldots, \sigma_L^2\right)}{\operatorname{argmax}} \; p\left(\boldsymbol{y} \middle| \hat{\boldsymbol{\theta}}_1, \ldots, \hat{\boldsymbol{\theta}}_M, \sigma_1^2, \ldots, \sigma_L^2\right)$$

and

$$\left(\hat{\boldsymbol{\theta}}_1, \ldots, \hat{\boldsymbol{\theta}}_M\right) = \underset{\left(\boldsymbol{\theta}_1, \ldots, \boldsymbol{\theta}_M\right)}{\operatorname{argmax}} \; p\left(\boldsymbol{y} \middle| \boldsymbol{\theta}_1, \ldots, \boldsymbol{\theta}_M, \hat{\sigma}_1^2, \ldots, \hat{\sigma}_L^2\right).$$

Being the likelihood a finite value, this iterative maximization is guaranteed to converge.

An initial estimate for the noise variance can be obtained from the signal energy

$$\hat{\sigma}_\ell^2 = \frac{1}{K} \sum_{k=1}^{K} \left(y_k^{(\ell)}\right)^2.$$

3.6 Additional details

The description of this section provides a rigorous description of the functioning of the proposed method and makes an implementation of the method possible using tools widely used in statistics. However, in our implementation, instead of computing (3) directly, we model the PDF of the observations by means of a factor graph (Loeliger *et al.* 2007). The factor graph formalism allows to derive a sufficient statistic and enables us to perform ML parameter estimation in a computationally attractive manner.

Further details of our implementation relying on factor graphs are given in Reller *et al.* (2011) and in Maranò *et al.* (2011).

3.7 Summary of contributions

The proposed method brings several improvements with respect to techniques currently in use.

(i) The proposed technique enables us to perform ML parameter estimation of wavefield parameter in a monochromatic wavefield relying on measurements corrupted by additive white Gaussian noise. The approach accounts for all the measurements and all the parameters jointly. Applicability of the proposed technique is not limited to the application presented in this paper. In particular, the technique allows to combine measurements from different types of sensors, and is readily extensible to waves with different polarization and to spherical wave fronts. The technique can cope with different sampling rates in each sensor.

(ii) Rayleigh wave ellipticity is retrieved including information about the prograde or retrograde particle motion. This is useful in mode separation and in the identification of singularities of the ellipticity (i.e. peaks and minima of the H/V representation of the ellipticity).

(iii) The wavefield decomposition addresses the simultaneous presence of multiple waves. By accounting for multiple waves, the estimation accuracy of each wave increases as parameters are iteratively re-estimated. This leads to the decomposition of the wavefield and allows the detection of weaker waves.

(iv) The proposed technique estimates the noise variance in each channel. This brings about various advantages. It enables us to use sensors of different technology and therefore with different noise levels. A misplaced or badly working sensor, will exhibit a higher noise level and will be automatically given less weight in the estimation process. Alternatively, it is possible to identify sensors having suspiciously high noise variance and perform a target check on that specific sensor.

(v) The issues of spatial sampling and array geometry are outside the scope of this work. However, it is known that the joint usage of all the sensor components leads to a benefit in terms of spatial aliasing (Hawkes & Nehorai 1998).

4 NUMERICAL RESULTS

4.1 Introduction

We present results of the proposed technique in different settings of increasing complexity. First, in Section 4.2, we compare the mean-squared error (MSE) of the proposed estimator with the Cramér-Rao bound (CRB) and the MSE of other estimators. In Section 4.3, we analyse a synthetic monochromatic wavefield with the aim of demonstrating the functioning of the algorithm in detail. In Section 4.4, we assess the performance of the algorithm on high-fidelity synthetics of the ambient vibrations wavefield developed during the SESAME project (Bonnefoy-Claudet *et al.* 2006a; Bard 2008). At last, in Sections 4.5 and in 4.6, two applications to two sites in Switzerland are presented. The data was recorded during seismic surveys performed by the Swiss Seismological Service in 2011.

We now give some details about the processing. All frequencies are processed independently. We apply no filtering to the recordings other than mean removal. The whole signal is split into blocks (time windows) of equal length within which the signal is assumed to be stationary. For comparison, we present results obtained using the three-components method for vertical, radial, and transverse component proposed in Fäh *et al.* (2008) using the same window length. We will refer to the three-components technique simply as 'classical beamforming'.

In the figures, dispersion curves are shown in wavenumber (in m^{-1}), versus frequency (in Hz). Ellipticity curves are shown both in ellipticity H/V and in ellipticity angle ξ versus frequency.

From the processing of long recordings, a large quantity of estimated wave parameters is available. In order to obtain a single picture representative of the results from the whole recording, we use the Parzen window method (Duda *et al.* 2001). The resulting grey-scale pictures depict with darker colour parameter values that are frequently estimated, with lighter colour less frequent values.

Empirical array resolution limits are computed according to Asten & Henstridge (1984). Given the minimum and the maximum array inter-station distance ($d_{\min}$ and $d_{\max}$ respectively), the minimum and maximum resolvable wavenumber are defined as

$$\kappa_{\min} = \frac{2\pi}{d_{\max}} \quad \text{and} \quad \kappa_{\max} = \frac{\pi}{d_{\min}}.$$

Such resolution limits are depicted graphically as thin dashed black lines.

4.2 Cramér-Rao bound analysis

We are interested in comparing the MSE of different estimators with the theoretical limit given by the CRB (Kay 1993). The CRB is a lower bound on the variance of unbiased estimators. We restrict ourselves to the analysis of the wavenumber κ as this is the parameter of most practical interest. For equal noise variance σ^2 in all signals, the element of the Fisher information matrix corresponding to the wavenumber κ is

$$\mathsf{E}\left[-\frac{\partial^2 \ln p(\boldsymbol{y}|\boldsymbol{\theta})}{\partial \kappa^2}\right] = \frac{\alpha^2 K \sum_{n=1}^{N} \left(\frac{\partial \boldsymbol{\kappa}^{\mathrm{T}} \boldsymbol{p}_n}{\partial \kappa}\right)^2}{2\sigma^2}. \tag{4}$$

When sensors are arranged regularly spaced on a circle, the Fisher information matrix is diagonal. Therefore, the MSE of any unbiased estimator is lower-bounded as

$$\mathsf{E}\left[(\hat{\kappa} - \mathsf{E}[\hat{\kappa}])^2\right] \geq \frac{2\sigma^2}{\alpha^2 K \sum_{n=1}^{N} \left(\frac{\partial \boldsymbol{\kappa}^{\mathrm{T}} \boldsymbol{p}_n}{\partial \kappa}\right)^2}. \tag{5}$$

We compare the MSE of three different estimators with the CRB by means of a numerical simulation. We consider the vertical and the radial component beamforming of Fäh *et al.* (2008) and the ML method of Section 3. We consider an uniform circular array of $N = 7$ sensors and a single Rayleigh wave with elliptic particle motion defined by $\xi = \pi/3$. Such a wave has most of the energy on the horizontal components.

In Fig. 2 the MSEs of the ML method and the classical beamforming are compared with the CRB for different signal-to-noise ratios (SNRs), where we define SNR $= \alpha^2/2\sigma^2$. At low SNR, where the noise dominates, the estimate is substantially random. The MSE saturates for decreasing SNR since the wavenumber estimate is constrained by the algorithm implementation to belong to a finite interval. As the SNR increases, the ML method always exhibits smaller MSE. For sufficiently large SNR, the ML method achieves the CRB. Even for high SNR the vertical component beamformer and the radial component beamformer do not achieve the CRB as they disregard the energy on the horizontal components or on the vertical component. The radial component beamformer exhibits in general smaller MSE than the vertical component beamformer because most of the energy of the wave is on the horizontal components (i.e. H/V $= \sqrt{3}$).

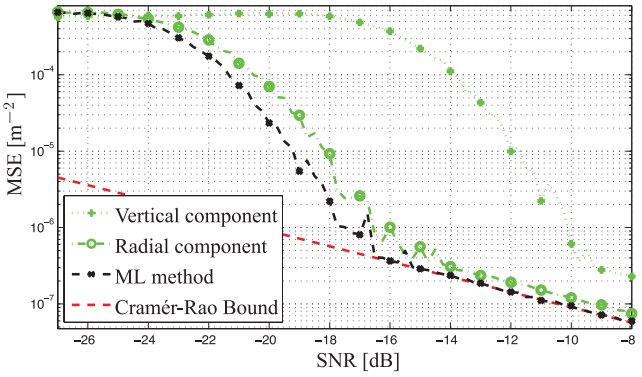

Figure 2. Comparison of the MSE of wavenumber estimates with the CRB at different SNR.

4.3 Monochromatic wavefield

In the first example, we generate a synthetic wavefield composed of two Love waves and two Rayleigh waves. All waves are monochromatic with known frequency of 1 Hz. We use an array of 14 triaxial sensors, 500 samples, and 5 s of observation. The measurements are corrupted by additive white Gaussian noise, with different variance in each channel. The true wavefield parameters are $\boldsymbol{\theta}_1^{(\mathrm{R})} = (0.9, 0, 0.03, \pi/4, \pi/4)^{\mathrm{T}}$, $\boldsymbol{\theta}_2^{(\mathrm{R})} = (0.7, \frac{\pi}{4}, 0.03, \pi/2, \pi/4)^{\mathrm{T}}$, $\boldsymbol{\theta}_3^{(\mathrm{L})} = (0.8, \frac{\pi}{3}, 0.04, -\pi/4)^{\mathrm{T}}$, and $\boldsymbol{\theta}_4^{(\mathrm{L})} = (0.2, \pi, 0.04, \pi)^{\mathrm{T}}$. The noise variances, the wavefield parameters, and the number and type of waves are unknown to the algorithm.

Fig. 3 shows how the estimates of the amplitudes α_ℓ converge toward their true values (dotted lines) after a sufficient number of iterations. The algorithm models additional waves at iterations 6, 11, and 14 as the likelihood (not shown) converges to a stable value. Similarly, Fig. 4 shows the estimates of the noise variances σ_ℓ^2. Sudden changes in estimated variance in the graph correspond to the inclusion of an additional wave in the graph. The improvements

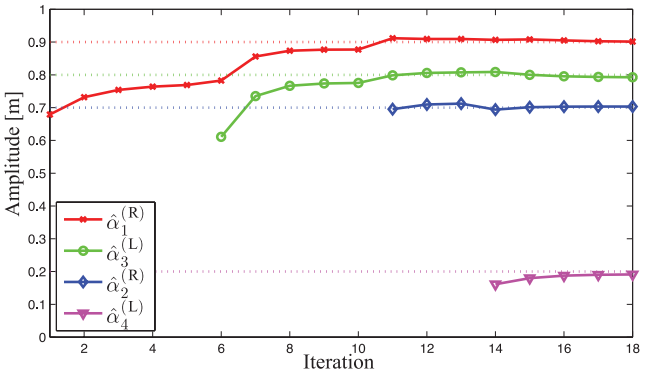

Figure 3. Estimated amplitudes at different iterations. The graph accounts for an additional wave at iteration 1, 6, 11, and 14. The dotted lines show the true amplitude of the waves.

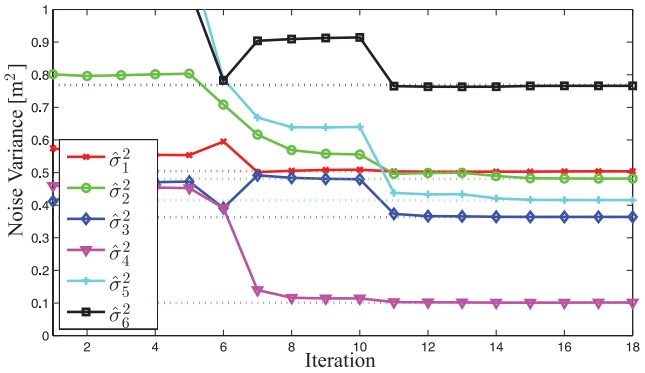

Figure 4. Estimated noise variances at different iterations. Only six channels are shown. The dotted lines show the value of the true variances.

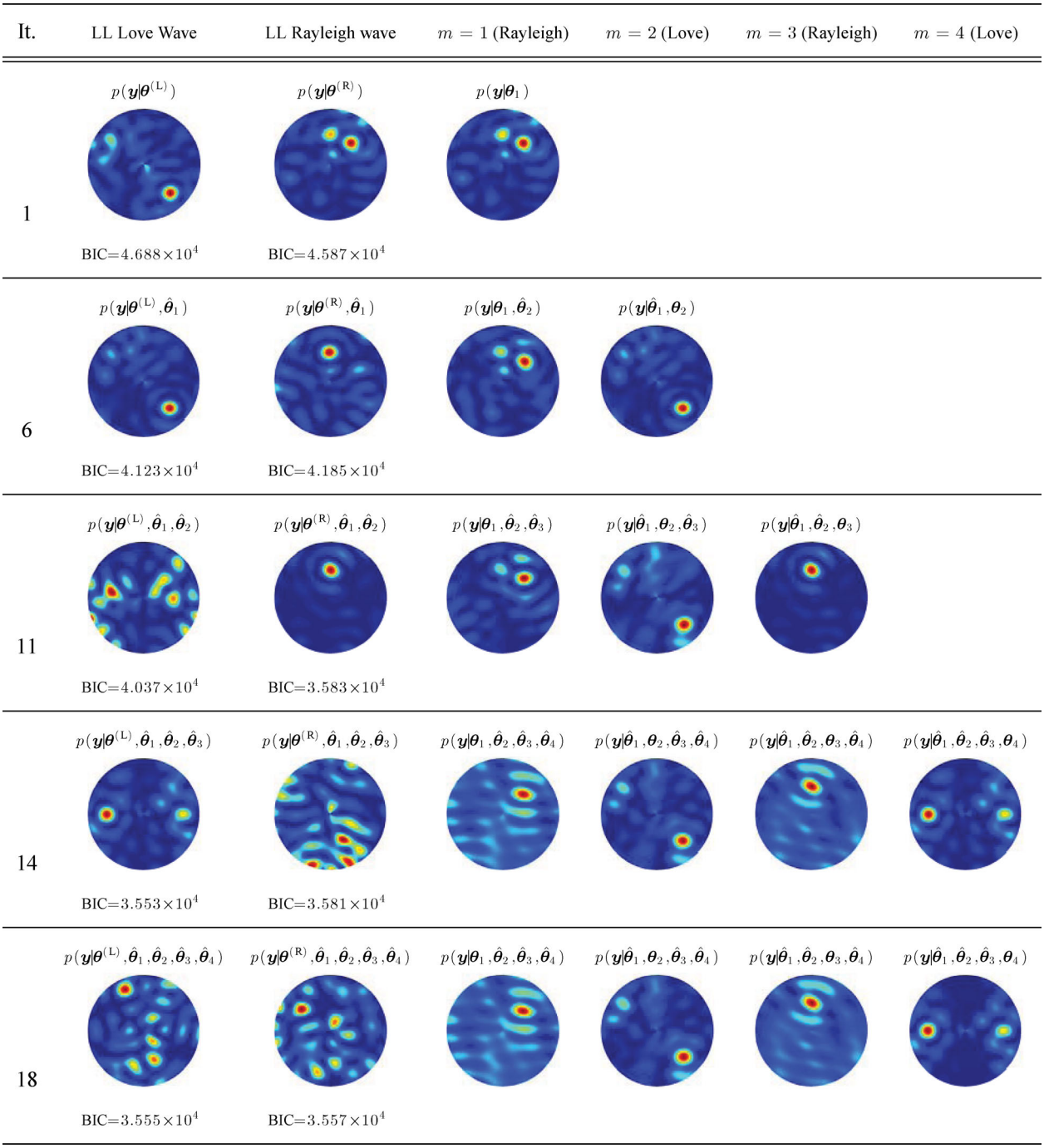

Figure 5. The normalized LL functions for Love waves and Rayleigh waves at different stages of the algorithm are depicted in polar coordinates as a function of wavenumber and azimuth (in each picture, the horizontal axis is $\kappa\cos\psi$ and the vertical axis is $\kappa\sin\psi$). The two leftmost columns show the LL of the residual wavefield, that is, the LL function of an additional wave while the parameters of the waves estimated in previous iterations are kept fixed. The other columns show the LL for the waves modelled by the algorithm. The BIC values shown motivates the choice of wave type and the termination of the algorithm.

in the estimated parameters between two wave inclusions, are due to repeated ML estimation of wave parameters and noise variances.

For the same experiment Fig. 5 depicts the (normalized) log-likelihood (LL) of Love waves and Rayleigh waves, at different iterations, as a function of wavenumber and azimuth. At iteration 1, the algorithm computes the likelihood function for Love waves and Rayleigh waves, as seen in the two leftmost columns. Two strong peaks are visible for Rayleigh waves, at azimuths $\pi/4$ and $\pi/2$. For Love waves, only one peak at azimuth $-\pi/4$ is visible. The algorithm chooses to model, as first wave $m = 1$, a Rayleigh wave. At iteration 6, the first two columns are again showing the likelihood of the data for Love waves and Rayleigh waves also modelling the Rayleigh wave previously estimated. For Rayleigh waves, now only a single peak is visible as the contribution from the first wave is already modelled. The depiction of the likelihood function for Love waves appears to be substantially unchanged. The second wave modelled

by the algorithm is a Love wave. At iteration 11, an additional Rayleigh wave is modelled. At iteration 14, only one Love wave remains in the wavefield (the wave parametrized by $\boldsymbol{\theta}_4^{(\mathrm{L})}$) and the associated peak, located at $\psi_4 = \pi$, is now visible. In the last iteration, all the four waves are modelled by the algorithm. At each step, wave type choice and algorithm termination are performed using the BIC.

4.4 SESAME model M2.1

We assess the performance of the algorithm on a synthetic model of a layer over a half-space developed during the SESAME project (Bonnefoy-Claudet *et al.* 2006a; Bard 2008). The recording has a duration of 400 s. The whole recording is split in non-overlapping windows of 2.5 s, each window is processed independently. An array of 14 sensors, with an aperture of roughly 80 meters is used. The geometry of this array is depicted in Fig. 6(a). Table 1 shows the geophysical properties of the model analysed (model M2.1 of the SESAME data set).

In the figures, the results for detected waves are overlaid with the theoretical dispersion curves and ellipticity curves computed from the structural model parameters in Table 1. For both dispersion and ellipticity curves, the red solid line refers to the fundamental mode, the dashed blue line to the first higher mode, the dot–dashed magenta line to the second higher mode, and the dotted green line to the third higher mode. Theoretical curves for Rayleigh wave and Love wave modes are depicted with the same colours but never appear in the same picture.

Fig. 6 depicts results of the method in (Fäh *et al.* 2008). The Rayleigh wave dispersion curves are seen on the vertical (Fig. 6b) and on the radial (Fig. 6c) components. Love wave dispersion curve is seen on the transverse component (Fig. 6d).

Fig. 7 depicts Love wave and Rayleigh wave dispersion curves as estimated with the ML technique. Figs 7(a) and (c) refer to the algorithm modelling at most one wave ($M_{\max} = 1$). Figs 7(b) and (d) refer to the joint modelling of at most three waves ($M_{\max} = 3$).

In general, we observe that the wavenumber estimates exhibit less scatter and less outliers when compared with the results depicted in Fig. 6. This is due to the joint usage of the three components and the use of the BIC.

Fig. 8 shows the result of ellipticity estimation. Figs 8(a) and (b) show the estimate of ellipticity in the H/V representation, for different $M_{\max}$. Figs 8(c) and (d) show the estimate of the ellipticity angle ξ. In these four figures all the estimated parameters are plotted and contribution of different modes are not distinguished as easily as for dispersion curves. For this reason, estimates corresponding to the first mode are isolated in the frequency–wavenumber plane and only the corresponding ellipticity estimates are shown in Fig. 9. In this latter figure the behaviour of the ellipticity of the fundamental mode can be understood more clearly. In Figs 9(c) and (d) it is possible to clearly identify the frequency at which the sense of rotation is changing (i.e. when $\xi = 0$). In addition, when comparing

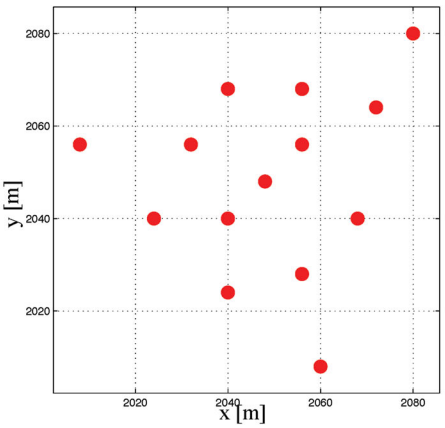

(a) Array layout with 14 sensors.

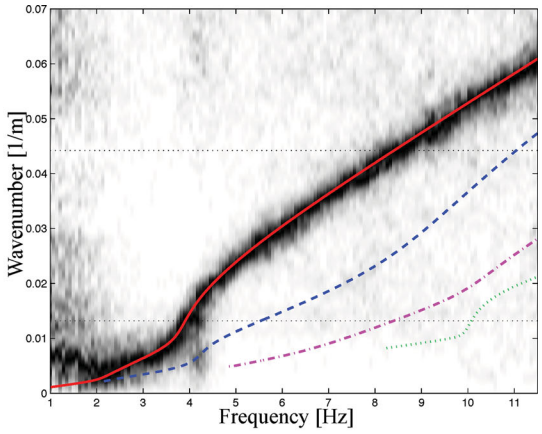

(b) Vertical component.

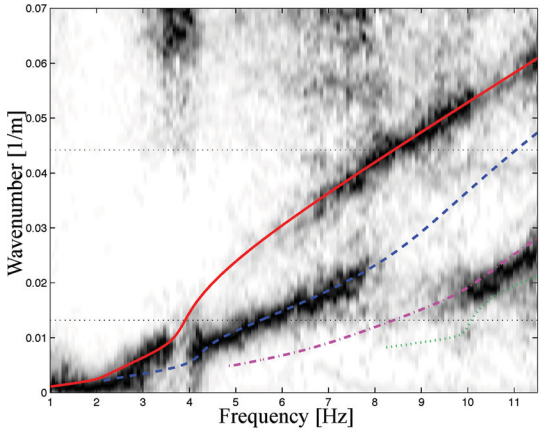

(c) Radial component.

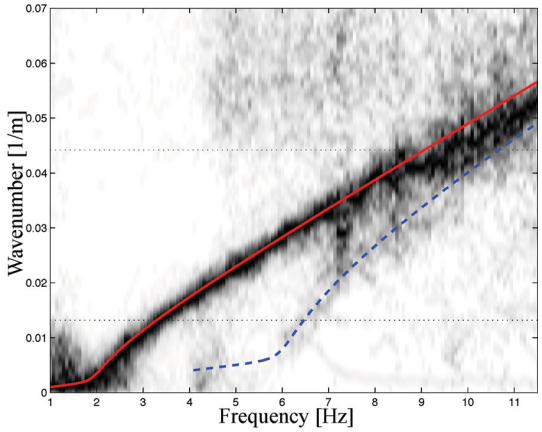

(d) Transverse component.

Figure 6. Rayleigh wave and Love wave dispersion curves obtained using the method in (Fäh *et al.* 2008) for the model M2.1.

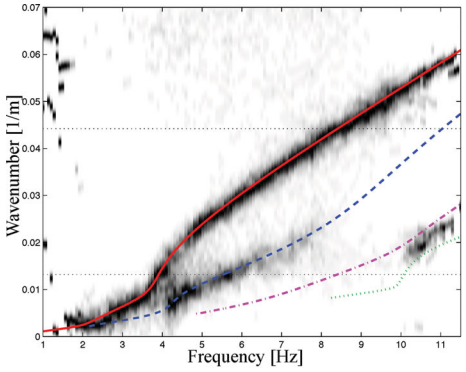

(a) Rayleigh wave dispersion curve, $M_{\max} = 1$.

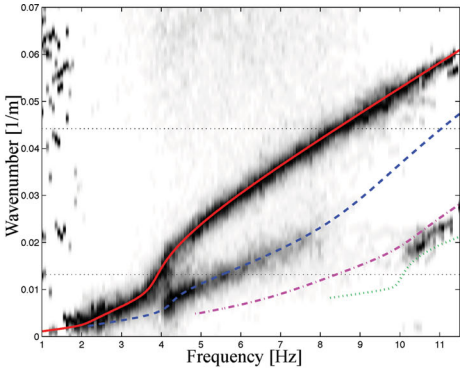

(b) Rayleigh wave dispersion curve, $M_{\max} = 3$.

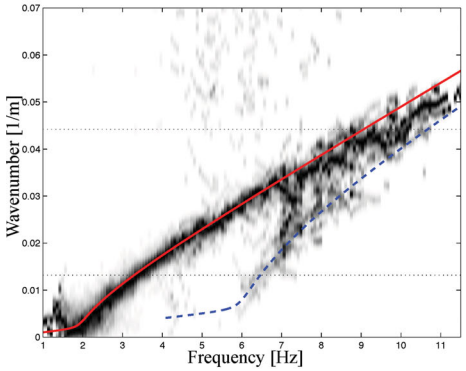

(c) Love wave dispersion curve, $M_{\max} = 1$.

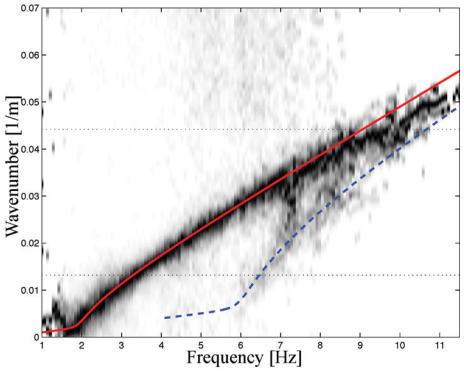

(d) Love wave dispersion curve, $M_{\max} = 3$.

Figure 7. Rayleigh and Love wave dispersion curves obtained using the ML technique for the model M2.1. Comparison between different number of waves.

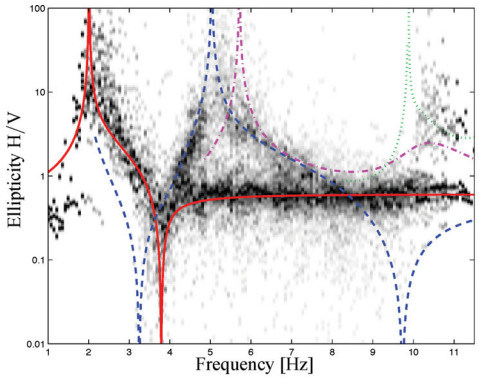

(a) Rayleigh wave ellipticity curve, $M_{\max} = 1$.

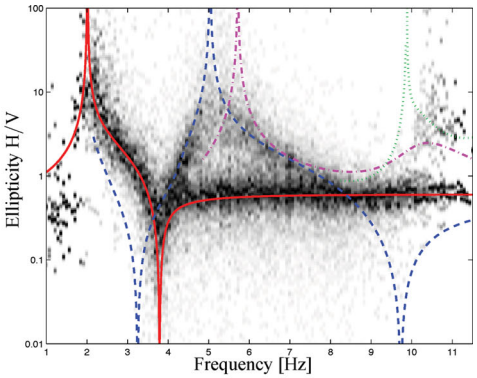

(b) Rayleigh wave ellipticity curve, $M_{\max} = 3$.

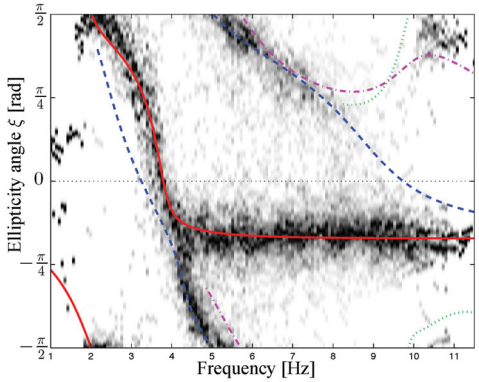

(c) Rayleigh wave ellipticity angle curve, $M_{\max} = 1$.

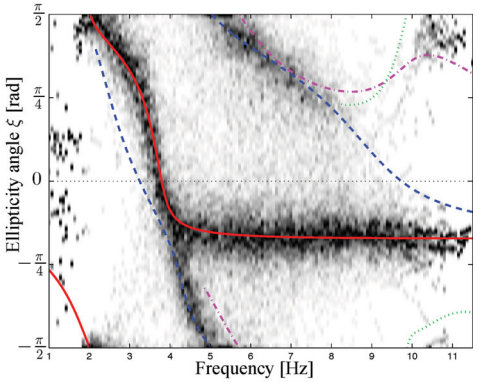

(d) Rayleigh wave ellipticity angle curve, $M_{\max} = 3$.

Figure 8. Rayleigh wave ellipticity curves obtained using the ML technique for the model M2.1. No selection on the wavenumber–frequency plane is performed.

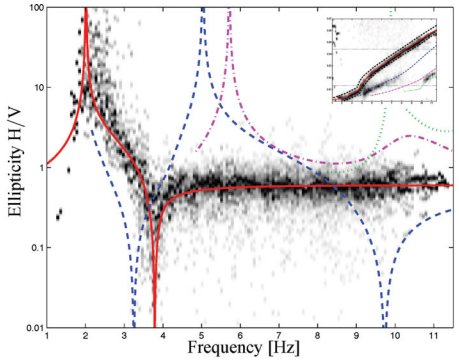

(a) Rayleigh wave ellipticity curve for fundamental mode, $M_{\max} = 1$.

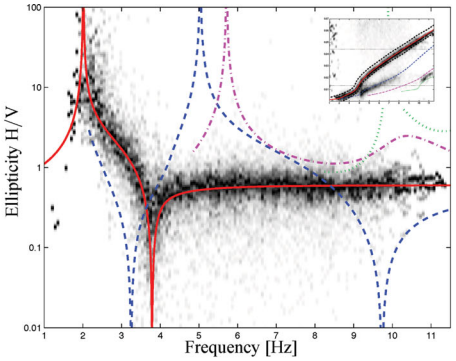

(b) Rayleigh wave ellipticity curve for fundamental mode, $M_{\max} = 3$.

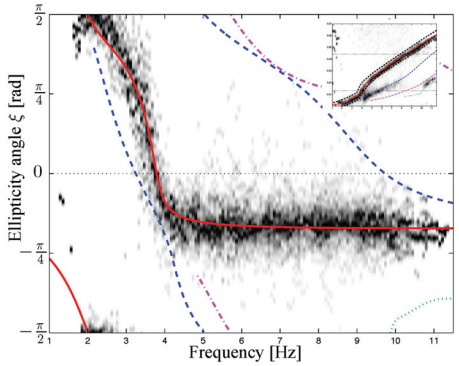

(c) Rayleigh wave ellipticity angle curve for fundamental mode, $M_{\max} = 1$.

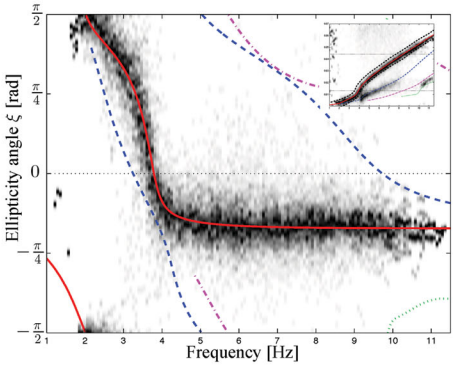

(d) Rayleigh wave ellipticity angle curve for fundamental mode, $M_{\max} = 3$.

Figure 9. Rayleigh wave ellipticity curves obtained using the ML technique for the model M2.1. The fundamental mode is selected in the wavenumber–frequency plane.

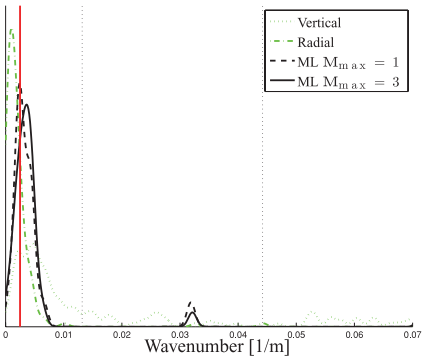

(a) 2.0 Hz.

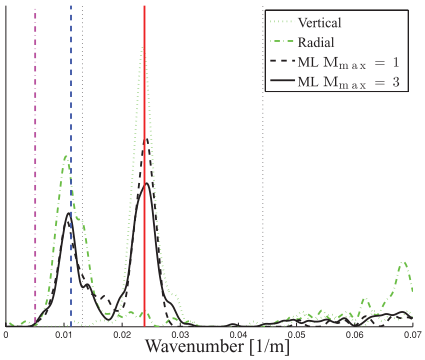

(b) 5.0 Hz.

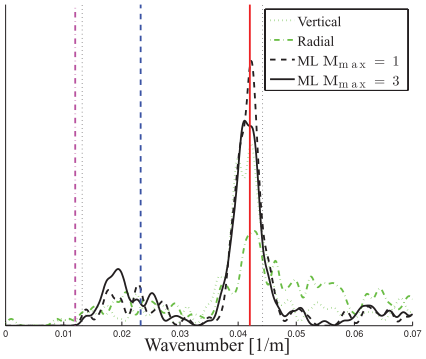

(c) 8.0 Hz.

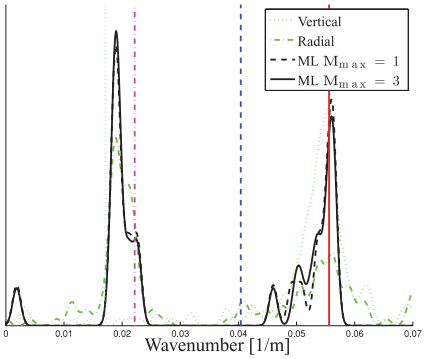

(d) 10.5 Hz.

Figure 10. The estimated wavenumber for Rayleigh waves at different frequencies using different methods. Theoretical wavenumbers are shown with vertical lines.

Fig. 9(c) with Fig. 9(d), it is possible to appreciate how the modelling of multiple waves makes it easier to follow the curves. Also, the estimated curve just above the resonance frequency of 2 Hz appears more accurate.

In Fig. 10 we compare the estimated wavenumbers for Rayleigh waves at different frequencies using different methods. Each figure shows the wavenumber estimates at a fixed frequency. The pictures in 10 can be compared with Figs 6(b), 6(c), 7(a), and 7(b). The theoretical wavenumbers are shown with vertical lines. Each curve is normalized to have unit area. At 2 Hz (Fig. 10a), the ML method better resolves the fundamental mode, which is substantially undetected by the vertical beamforming and detected with some bias by the radial beamforming. At 5.0 Hz (Fig. 10b), the proposed method detects both the fundamental and the first higher mode. The two modes are detected separately by the vertical and the radial beamforming due to the different ellipticity of the different modes. At 8.0 Hz (Fig. 10c), the fundamental mode is more clearly resolved by the ML method. At 10.5 Hz (Fig. 10c), the ML method detects both the fundamental and the second higher mode. Note that the bias in estimation on the second higher mode is shared by all the estimators. Indeed the estimated mode might be a mixture of the second and the third higher mode. In general, the proposed method also exhibit a smaller amount of outliers.

4.5 Brigerbad, Wallis

The Brigerbad site is located in the Rhone valley, a deep Alpine valley, in southern Switzerland. An array of 12 Lennartz 5 s triaxial sensors is used. The layout of the array is depicted in Fig. 11(a). The whole recording is 58 minutes long and it is split into 10 s windows which are processed independently. Sampling rate is 200 Hz.

Fig. 11 shows the results of the analysis performed using the method in Fäh *et al.* (2008). The fundamental mode of the Rayleigh wave is visible on the vertical component (Fig. 11b). The first higher mode of the Rayleigh wave is visible on the radial component (Fig. 11c) and only weakly on the vertical component. The fundamental mode of the Love wave is visible on the transverse component (Fig. 11d).

Fig. 12 shows the results of the analysis performed using the ML technique described in this paper. Both the fundamental mode and the first higher mode of the Rayleigh wave are visible in Fig. 12(b). The fundamental mode of the Love wave is visible in Fig. 12(a).

In Fig. 12 Rayleigh wave ellipticity curves are shown for different modes and different representations. The ellipticity of the fundamental mode is shown in Figs 12(c) and (d). We emphasize how the zero of the H/V curve, just above 6 Hz, is very clearly identified by looking at the ellipticity angle representation of Fig. 12(d).

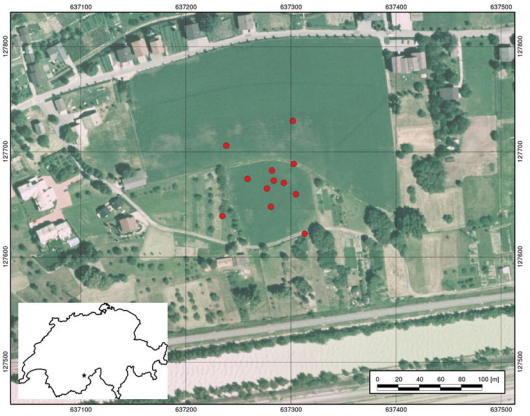

(a) Geometry of the sensor array used in the Brigerbad survey. The inlet pinpoints the location of the array within Switzerland. The geographic coordinates are Swiss coordinates (CH1903).

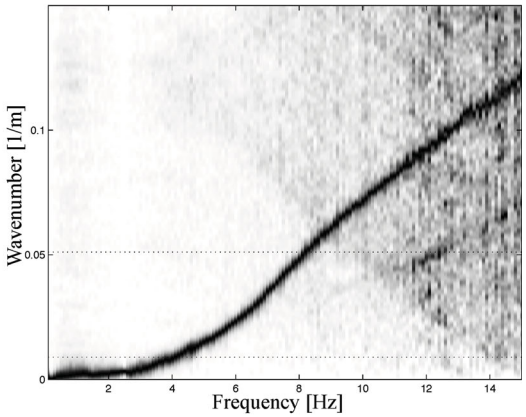

(b) Vertical component.

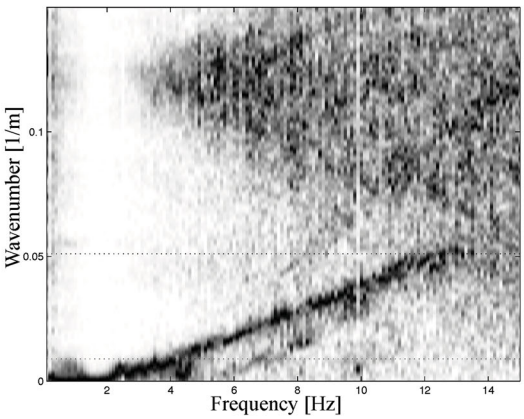

(c) Radial component.

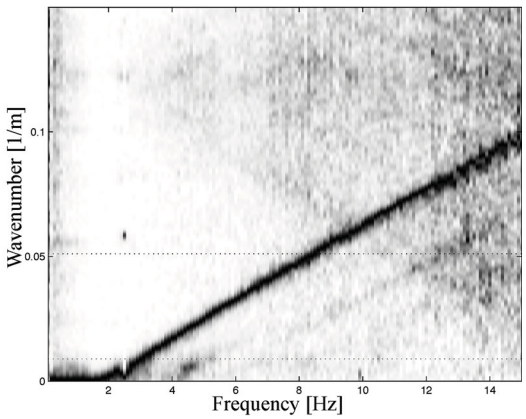

(d) Transverse component.

Figure 11. Rayleigh wave and Love wave dispersion curves obtained using the method in (Fäh *et al.* 2008) for Brigerbad survey.

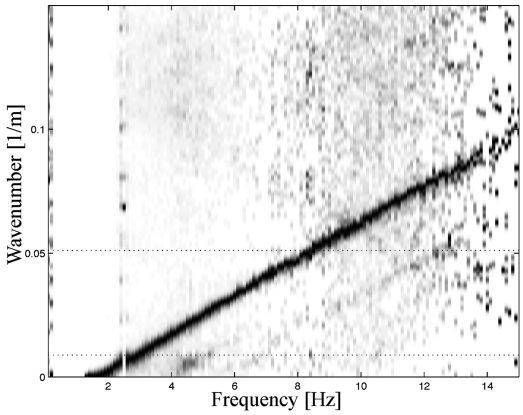

(a) Love wave dispersion curve.

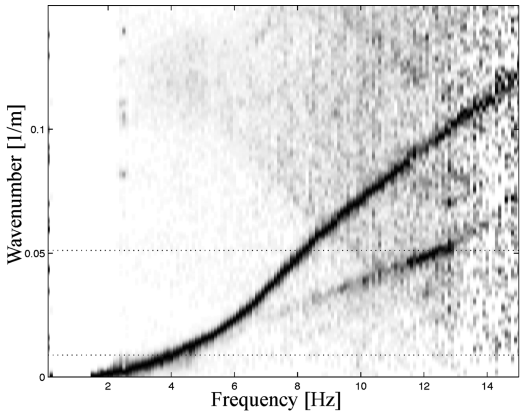

(b) Rayleigh wave dispersion curve.

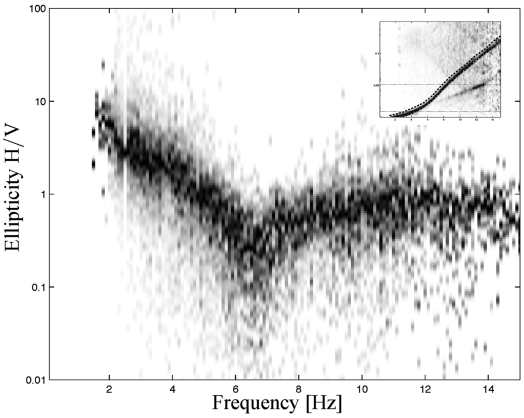

(c) Rayleigh wave ellipticity curve for fundamental mode.

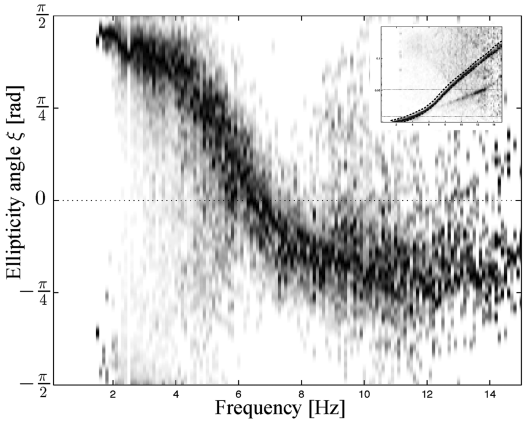

(d) Rayleigh wave ellipticity angle curve for fundamental mode.

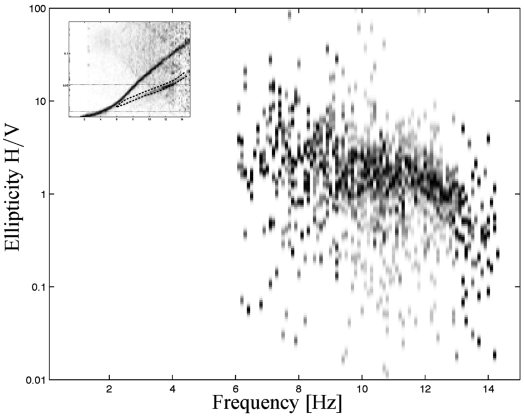

(e) Rayleigh wave ellipticity curve for first higher mode.

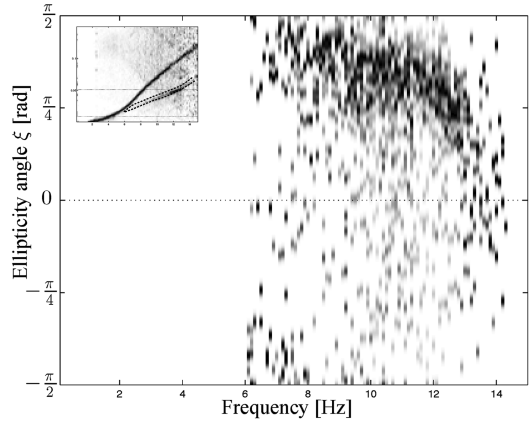

(f) Rayleigh wave ellipticity angle curve for first higher mode.

Figure 12. Dispersion curves and ellipticity curves obtained using the ML technique for Brigerbad survey. These results are obtained from a single processing with $M_{\max} = 3$.

Analogously, in Figs 12(e) and (f) the Rayleigh wave ellipticity for the first higher mode is shown.

4.6 Rheintal, St. Gallen

The Rheintal site is located in the Rhein valley, an Alpine valley, in eastern Switzerland. An array of 13 Lennartz 5 s triaxial sensors is used. The layout of the array is depicted in Fig. 13(a). The whole recording is almost six hours long and it is split in 10 s windows which are processed independently. Sampling rate is 200 Hz.

Fig. 13 shows the results of the analysis performed using the method in Fäh *et al.* (2008). The fundamental mode of the Rayleigh wave is visible only in the vertical component (Fig. 13b). The Love wave fundamental mode is weakly visible on the transverse component. The analysis of the radial component brings no clear information.

Fig. 14 shows the results of the analysis performed using the ML technique described in this paper. The fundamental mode of the Rayleigh wave is visible in Fig. 14(b). The fundamental mode of the Love wave is visible in Fig. 14(a). We note that the Love

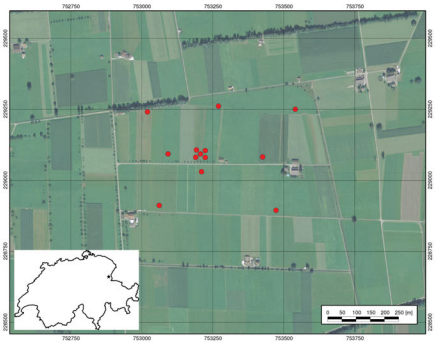

(a) Geometry of the sensor array used in the Rheintal survey. The inlet pinpoints the location of the array within Switzerland. The geographic coordinates are Swiss coordinates (CH1903).

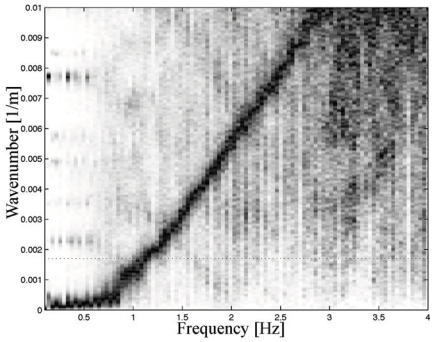

(b) Vertical component.

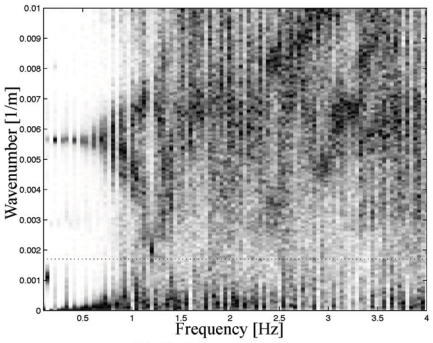

(c) Radial component.

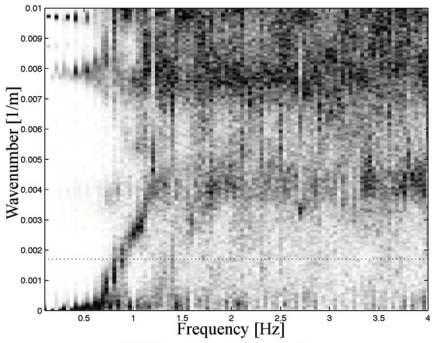

(d) Transverse component.

Figure 13. Rayleigh wave and Love wave dispersion curves obtained using the method in (Fäh *et al.* 2008) for the Rheintal survey.

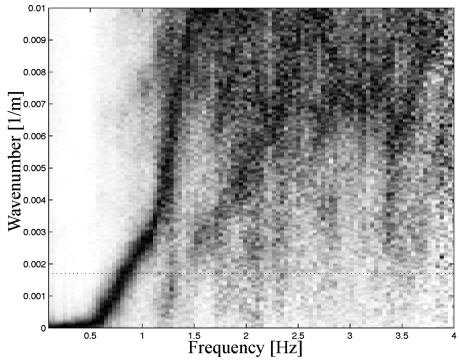

(a) Love wave dispersion curve.

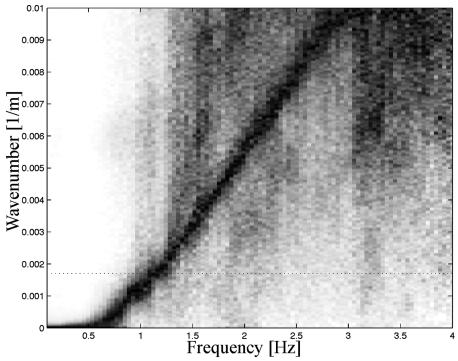

(b) Rayleigh wave dispersion curve.

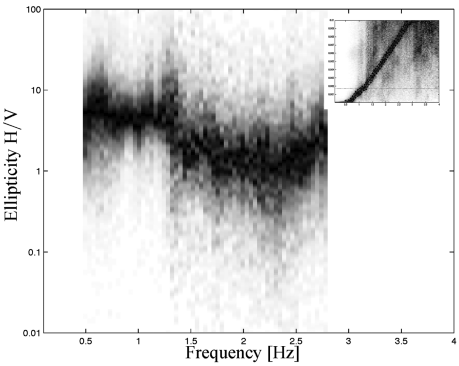

(c) Rayleigh wave ellipticity curve for fundamental mode.

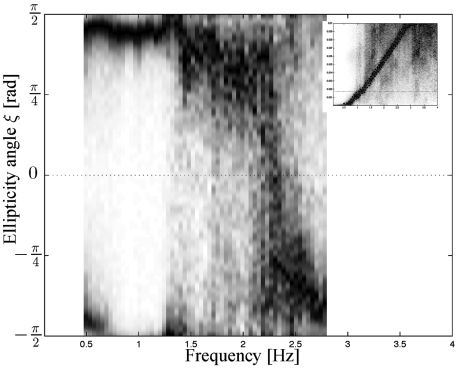

(d) Rayleigh wave ellipticity angle curve for fundamental mode.

Figure 14. Rayleigh wave and Love wave dispersion curves obtained using the ML technique for the Rheintal survey. $M_{\max} = 3$.

wave dispersion curve is now clearly visible with the ML method. Since the ML technique chooses between Love wave and Rayleigh wave adaptively, the algorithm tends to model the stronger waves first, then removes its contribution, allowing the detection of weaker signals (in this instance the fundamental mode Love wave), and the final elaboration is improved.

In Figs 14(c) and (d) Rayleigh wave ellipticity curves of the fundamental mode are shown in the different representations. We emphasize how the zero of the H/V curve around 2.5 Hz is again clearly identified by looking at the ellipticity angle representation of Fig. 14(d).

5 CONCLUSIONS

In this paper, we have presented an application to the analysis of surface waves from ambient vibrations recording of a recently developed technique for array processing of the seismic wavefield.

The technique performs ML wavefield parameter estimation accounting for all the measurements and all the parameters jointly. The technique allows to model the simultaneous presence of multiple waves. Notably, we provide an ML estimate of Rayleigh wave ellipticity and the sense of particle rotation (prograde versus retrograde).

We evaluated the performance of this technique on high-fidelity synthetic data set from the SESAME project and on real data from two surveys. This method improves estimates of Love wave and Rayleigh wave dispersion curves, and allows for an estimate of Rayleigh wave ellipticity. We have also shown that modelling multiple waves enables us to detect weaker waves that are not visible with traditional methods.

Further developments of the method will include an adaptive window selection and the extension to other wave types such body waves and resonances.

ACKNOWLEDGMENTS

The authors wish to thank Dr J. Burjánek, Dr C. Cauzzi, Q. Keeris, P. Galvez, Dr C. Michel, Dr V. Poggi and Dr J. Revilla for their invaluable assistance during the Rheintal measurement campaign. We also wish to thank Spectraseis AG for providing technical support during the same survey. Concerning the Brigerbad data set, the authors wish to thank Dr J. Burjánek and Dr C. Michel. This work is supported in part by the Swiss Commission for Technology and Innovation under project 9260.1 PFIW-IW.

REFERENCES

Asten, M.W. & Henstridge, J.D., 1984. Array estimators and the use of microseisms for reconnaissance of sedimentary basins, *Geophysics,* **49**(11), 1828–1837.

Bard, P.-Y., 2008. SESAME: site effects assessment using ambient excitations, http://sesame-fp5.obs.ujf-grenoble.fr (last accessed 2012 July 24).

Bonnefoy-Claudet, S., Cornou, C., Bard, P.-Y., Cotton, F., Moczo, P., Kristek, J. & Fäh, D., 2006a. H/V ratio: a tool for site effects evaluation. results from 1-D noise simulations, *Geophys. J. Int.,* **167**(2), 827–837.

Bonnefoy-Claudet, S., Cotton, F. & Bard, P.-Y., 2006b. The nature of noise wavefield and its applications for site effects studies: a literature review, *Earth-Sci. Rev.,* **79**(3-4), 205–227.

Capon, J., 1969. High-resolution frequency-wavenumber spectrum analysis, *Proc. IEEE,* **57**(8), 1408–1418.

Christoffersson, A., Husebye, E.S. & Ingate, S.F., 1988. Wavefield decomposition using ML-probabilities in modelling single-site 3-component records, *Geophys. J. Int.,* **93**(2), 197–213.

Cornou, C., Bard, P.-Y. & Dietrich, M., 2003. Contribution of dense array analysis to the identification and quantification of basin-edge-induced waves. Part I: methodology, *Bull. seism. Soc. Am.,* **93**(6), 2604–2623.

Duda, R.O., Hart, P.E. & Stork, D.G., 2001. *Pattern Classification,* John Wiley & Sons, New York, NY.

Fäh, D., Stamm, G. & Havenith, H.-B., 2008. Analysis of three-component ambient vibration array measurements, *Geophys. J. Int.,* **172**(1), 199–213.

Hawkes, M. & Nehorai, A., 1998. Acoustic vector-sensor beamforming and capon direction estimation, *IEEE Trans. Signal Process.,* **46**(9), 2291–2304.

Kay, S.M., 1993. *Fundamentals of Statistical Signal Processing: Estimation Theory,* Prentice Hall, Upper Saddle River, NJ.

Lacoss, R., Kelly, E. & Toksöz, M., 1969. Estimation of seismic noise structure using arrays, *Geophysics,* **34**(1), 21–38.

Loeliger, H.-A., Dauwels, J., Hu, J., Korl, S., Ping, L. & Kschischang, F.R., 2007. The factor graph approach to model-based signal processing, *Proc. IEEE,* **95**(6), 1295–1322.

Malischewsky, P.G., Lomnitz, C., Wuttke, F. & Saragoni, R., 2006. Prograde Rayleigh-wave motion in the valley of Mexico, *Geofísica Internacional,* **45,** 149–162.

Malischewsky, P.G., Scherbaum, F., Lomnitz, C., Tuan, T.T., Wuttke, F. & Shamir, G., 2008. The domain of existence of prograde Rayleigh-wave particle motion for simple models, *Wave Motion,* **45,** 556–564.

Maranò, S., Reller, C., Fäh, D. & Loeliger, H.-A., 2011. Seismic waves estimation and wave field decomposition with factor graphs, in *Proceedings of the IEEE International Conference on Acoustics, Speech, and Signal Processing,* Prague, Czech Republic.

Okada, H., 1997. *The Microtremor Survey Method,* Society of Exploration Geophysicists, Tulsa, OK.

Poggi, V. & Fäh, D., 2010. Estimating Rayleigh wave particle motion from three-component array analysis of ambient vibrations, *Geophys. J. Int.,* **180**(1), 251–267.

Reller, C., Loeliger, H.-A. & Maranò, S., 2011. Multi-sensor estimation and detection of phase-locked sinusoids, in *Proceedings of the IEEE International Conference on Acoustics, Speech, and Signal Processing,* Prague, Czech Republic.

Schmidt, R.O., 1986. Multiple emitter location and signal parameter estimation, *IEEE Trans. Antennas Propag.,* **3**(3), 276–280.

Schwarz, G.E., 1978. Estimating the dimension of a model, *Ann. Stat.,* **6**(2), 461–464.

Sheriff, R.E. & Geldart, L.P., 1995. *Exploration Seismology,* Cambridge University Press, Cambridge.

Tarantola, A., 2004. *Inverse Problem Theory and Methods for Model Parameter Estimation,* SIAM, Philadelphia, PA.

Tokimatsu, K., 1997. Geotechnical site characterization using surface waves, in *Proceedings of the 1st International Conference on Earthquake Geotechnical Engineering,* pp. 1333–1368, ed. Ishihara, K., Balkema, Rotterdam.

Van Trees, H.L., 2002. *Optimum Array Processing: Part IV of Detection, Estimation, and Modulation Theory,* John Wiley & Sons, Inc., New York, NY.